

A radial velocity survey of low Galactic latitude structures – I. Kinematics of the Canis Major dwarf galaxy

N. F. Martin,¹^{*} R. A. Ibata,¹ B. C. Conn,² G. F. Lewis,² M. Bellazzini³ and M. J. Irwin⁴

¹*Observatoire de Strasbourg, 11, rue de l'Université, F-67000, Strasbourg, France*

²*Institute of Astronomy, School of Physics, A29, University of Sydney, NSW 2006, Australia*

³*INAF – Osservatorio Astronomico di Bologna, Via Ranzani 1, 40127, Bologna, Italy*

⁴*Institute of Astronomy, Madingley Road, Cambridge CB3 0HA*

Accepted 2005 June 21. Received 2005 June 17; in original form 2005 April 1

ABSTRACT

As part of a radial velocity survey of low Galactic latitude structures that we undertook with the 2dF spectrograph on the Anglo-Australian Telescope, we present the radial velocities of more than 1500 red giant branch and red clump stars towards the centre of the Canis Major dwarf galaxy. With a mean velocity of $72 \pm 7 \text{ km s}^{-1}$ at a heliocentric distance of 5.5 kpc and $114 \pm 2 \text{ km s}^{-1}$ at 8.5 kpc, these stars present a peculiar distance – radial velocity relation that is unlike that expected from thin or thick disc stars. Moreover, they belong to a kinematically cold population with an intrinsic dispersion that may be as low as $11^{+3}_{-1} \text{ km s}^{-1}$. A comparison of the velocity distribution obtained in this work with previous studies shows the importance of using our new reduction pipeline and averaging the velocities obtained from different templates.

The radial velocity distribution is used to select Canis Major stars in the UCAC2.0 proper motion catalogue and derive proper motions in Galactic coordinates of $(\mu_l, \mu_b) = (-3.6 \pm 0.8 \text{ mas yr}^{-1}, 1.5 \pm 0.4 \text{ mas yr}^{-1})$ for the dwarf galaxy, which after correcting for the reflex solar motion along this line of sight gives $(\mu'_l, \mu'_b) = (-6.8 \pm 0.8 \text{ mas yr}^{-1}, 0.8 \pm 0.4 \text{ mas yr}^{-1})$, corresponding to a prograde orbit with a tangential velocity of $\sim 235 \text{ km s}^{-1}$ at the average distance of $\sim 7.2 \text{ kpc}$. All these kinematic constraints can be reproduced in simulations of the accretion of a dwarf on to the Galactic disc. Such a process could also be responsible for the Monoceros Ring that has recently been shown to encompass the Galactic disc. However, without constraints on the kinematics of the tidal arms emerging from the Canis Major dwarf, it is not yet possible to definitively prove a link between the two structures.

Key words: Galaxy: structure – galaxies: individual: Canis Major – galaxies: interactions.

1 INTRODUCTION

The advent of all sky surveys is revealing numerous structures toward the edge of the Galactic disc. The Sloan Digital Sky Survey (SDSS) revealed a ring-like structure, the so-called Monoceros Ring (Mon Ring), that was later shown to encompass part of the Galactic disc (e.g. Newberg et al. 2002; Yanny et al. 2003; Ibata et al. 2003; Crane et al. 2003; Conn et al. 2005a). Similarly, the 2MASS infrared catalogue was used to unveil the existence of a diffuse structure in the direction of the Triangulum and Andromeda constellations (Rocha-Pinto et al. 2004) and to reveal the presence of a dwarf galaxy below the disc in the Canis Major (CMA) constellation (Martin et al. 2004a, hereafter Paper I).

This latter structure was first identified as an overdensity of red giant branch (RGB) stars located just below the Galactic disc at $(l, b) \sim (240^\circ, -8^\circ)$. The analysis of archival colour–magnitude diagrams (CMD) of open clusters that are fortuitously located around this region confirmed this stellar overdensity extends over 20° in Galactic longitude (Bellazzini et al. 2004, hereafter Paper II) while main-sequence fitting revealed this population has an intermediate age (4–10 Gyr). Applying a tip of the RGB algorithm yielded a distance of $7.2 \pm 0.3 \text{ kpc}$ for the dwarf (Martin et al. 2004b, hereafter Paper III), making it the closest galaxy from the Sun. Interestingly, CMA lies at a comparable Galactocentric distance to the Sagittarius dwarf.

As an alternative interpretation, Momany et al. (2004) explain this stellar structure as a signature of the Galactic warp. Using the UCAC2.0 proper motion catalogue, they derive a proper motion that, within sizable uncertainties, is compatible with a Galactic population on a prograde disc-like orbit: $[\mu_\alpha \cos(\delta), \mu_\delta] = (-1.7 \pm$

^{*}E-mail: martin@astro.u-strasbg.fr

2 mas yr⁻¹, 3.1 ± 2 mas yr⁻¹). However, comparison of deep optical photometry CMDs with Galactic models reveals the structure is incompatible with known Galactic structure (Paper II) and yields a narrow extent on the line of sight, with a FWHM of only 1.92 kpc (Martínez-Delgado et al. 2005), difficult to achieve with a conventional warp. Moreover, the radial velocities of a small sample of RGB stars in CMa show they belong to a kinematically cold population that, if on a circular orbit, would rotate around the Milky Way at a rotational velocity of ~ 160 km s⁻¹ that is low for disc stars (Paper III).

The existence of a dwarf so close to the Galactic disc, along with structures like the Mon Ring and the TriAnd feature raises questions on their role in the formation of the Galactic (thick) disc (Paper I). However, answering this question first requires us to determine if there is a link between these three structures. Peñarrubia et al. (2005) used all known distance, radial velocity and proper motion data to constrain simulations of the formation of the Mon Ring by an accretion event. Interestingly, they predict the progenitor of the Ring should be located around the position of CMa ($l \sim 245^\circ$ and $b \sim -18^\circ$) but at twice the estimated distance of the CMa dwarf. Therefore, it remains unclear whether the two structures are linked or not.

This paper is the first in a series that aims at analysing the kinematics of these different low latitude Galactic structures. In particular, we aim at constraining the orbit of the accreted dwarf and determining if the Mon Ring could be a by-product of this accretion. Here, we present our complete sample of radial velocities of RGB and red clump (RC) stars in the CMa overdensity and show it presents non-Galactic features. In Section 2 we discuss the data set we use for our radial velocity study of Section 3. These radial velocities are used in Section 4, to select CMa stars from the UCAC2.0 catalogue and determine the proper motion of the dwarf. The obtained kinematics are then used in Section 5 to constrain simulations of the accretion of a dwarf on to the Galactic disc. Conclusions are presented in Section 6.

In the following, all the J , H , K magnitudes from 2MASS have been corrected from extinction using the maps from Schlegel, Finkbeiner & Davis (1998), modified by the asymptotic correction from Bonifacio, Monai & Beers (2000). We also assume that the Solar radius is $R_\odot = 8$ kpc, that the LSR circular velocity is 220 km s⁻¹, and that the peculiar motion of the Sun is ($U_0 = 10.00$ km s⁻¹, $V_0 = 5.25$ km s⁻¹, $W_0 = 7.17$ km s⁻¹; Dehnen & Binney 1998). Except when stated otherwise, the radial velocities are the observed Heliocentric radial velocity, not corrected for the motion of the Sun.

2 OBSERVATIONS AND REDUCTION

The aim of the low Galactic latitude survey we undertook with the 2dF spectrograph was to determine the kinematics of the different asymmetries that appear in the distribution of RGB stars (figs 3–5 of Paper I) and in particular kinematics of the CMa dwarf galaxy. Hence, four fields out of the ~ 15 in our survey were directly aimed at the centre of the CMa overdensity as found in Paper I: (l, b) = ($240.0^\circ, -4.8^\circ$), (l, b) = ($240.0^\circ, -6.8^\circ$), (l, b) = ($240.0^\circ, -8.8^\circ$) and (l, b) = ($240.0^\circ, -10.8^\circ$). We also observed another field on the opposite side of the Galactic disc, at (l, b) = ($240.0^\circ, +8.8^\circ$) to provide a reference to compare with the CMa fields.

In each two-degree field, our primary targets were the RGB stars selected from sample A of Paper I and within 4–20 kpc from the

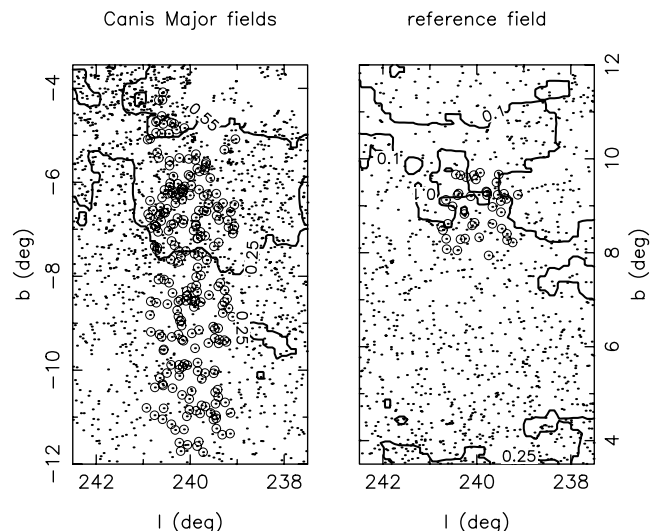


Figure 1. Map of the target RGB stars for the CMa region (left panel) and the reference field (right panel). All RGB stars of these regions are shown as dots and target stars are circled. Extinction contours for $E(B - V) = 0.1, 0.25$ and 0.55 are also shown as thick lines. Target RC stars follow the distribution of target RGB stars but are not shown to avoid overcrowding the plots.

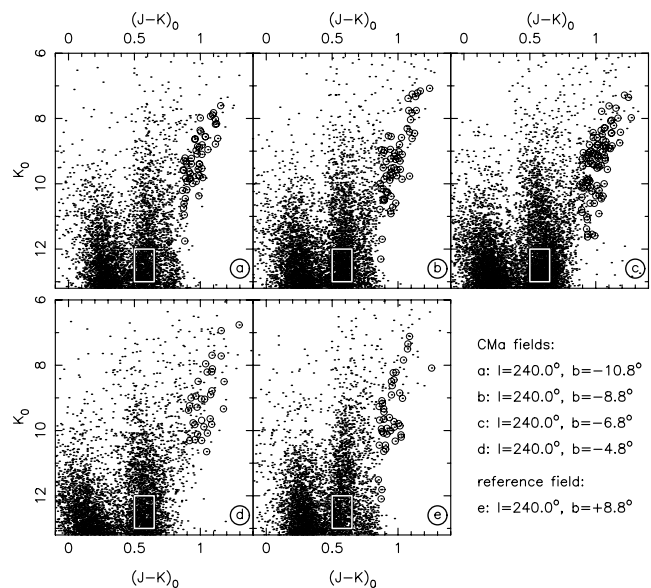


Figure 2. 2MASS infrared CMDs of the four target fields around CMa (a–d panels) and the symmetric field above the Galactic disc (panel e). On each panel, the observed RGB stars are shown as circled dots and the selection box from which RC stars were chosen is drawn in white.

Sun.¹ These stars are highlighted on the map of sample A stars shown on Fig. 1 and mainly fall in regions of reasonable extinction ($E(B - V) < 0.4$). Only the field closest to the Galactic disc with $-5.8^\circ < b < -3.8^\circ$ suffers from significant variable extinction. The target stars are also shown on the CMD of each field in Fig. 2. As the CMa structure has a prominent RC (see Papers I and II),

¹ We recall that the distance to RGB stars were determined by the photometric parallax technique presented by Majewski et al. (2003) that we applied to a sample of CMa stars in Paper III.

we placed the remaining fibres to observe a sample of RC stars at the estimated distance of CMa: $5 \text{ kpc} < D_{\odot} < 8 \text{ kpc}$, assuming a distance of 7.2 kpc for the bulk of the overdensity (Paper III) and an absolute magnitude of $M_K = -1.5 \pm 0.2$ for the RC population of CMa (Paper II), independent of colour which was chosen within the range $0.5 < J - K < 0.65$. The corresponding selection box has also been drawn on Fig. 2. It can be seen that even in fields with increasing extinction values (panels *c* and *d*), the selection box remains centred on the RC zone, hinting at a good extinction correction for stars at this distance.

The observations were obtained during the nights of 2004 April 7–12. We employed two different spectrograph settings, with the 1200V grating on spectrograph 1 (covering $4600\text{--}5600 \text{ \AA}$ at 1 \AA pixel^{-1}) and with the 1200R grating on spectrograph 2 (covering $8000\text{--}9000 \text{ \AA}$, also at 1 \AA pixel^{-1}). The observations have been reduced using the 2dF Data Reduction package provided by the AAO (Taylor et al. 1996) for the correction from the flat fields, the extraction of the spectrum of each fibre and the sky subtraction.

2.1 Reduction of first spectrograph spectra

We use a custom-made reduction pipeline to correct the asymmetry of the line spread function (LSF) of the 2dF with the first spectrograph settings. This pipeline is described in detail in Martin et al. (2005) and can be summarized as follows.

- (i) The asymmetry of the LSF is modelled across the CCD for each observed field.
- (ii) The spectrum of a given fibre is calibrated using the corresponding LSF model.
- (iii) For each observed spectrum, the model is also used to generate template spectra. Hence, when doing a Fourier cross-correlation to determine the radial velocity of an observed star, both the observed spectrum and the templates are deformed in an identical way. We have shown that this procedure ensures that we avoid systematic offsets higher than $\pm 5 \text{ km s}^{-1}$ due to deformations of the LSF.

Each observed spectrum was cross-correlated with up to nine different templates of giant stars, from K4III to M4III spectral types, generated from high resolution spectra from the UVES Paranal Observatory Project (Bagnulo et al. 2003, see Martin et al. 2005 and Table 1 for the list of templates). RGB stars are cross-correlated with all nine templates and have typical uncertainties of $\sim 4\text{--}7 \text{ km s}^{-1}$ for each derived radial velocity while RC stars are cross-correlated with the first five templates (from K4III to M0III spectral type), because their spectra are unlikely to correspond to a higher spectral type,

Table 1. Templates used for cross-correlation of first spectrograph observations. The high-resolution spectra of these stars are extracted from the UVES Paranal Observatory Project (Bagnulo et al. 2003).

Star	Spectral type	Radial velocity (km s^{-1}) ^a
HD 145206	K4III	−46.0
HD 167818	K5III	−16.9
HD 149447	K6III	−2.1
HD 89736	K7III	16.0
HD 92305	M0III	−22.4
HD 102212	M1III	50.7
HD 120052	M2III	64.2
HD 224935	M3III	−11.8
HD 11695	M4III	1.5

^aObtained using the SIMBAD data base, operated at CDS, Strasbourg, France.

and have typical uncertainties of $\sim 8\text{--}15 \text{ km s}^{-1}$ for each template. Instead of choosing one of the template-specific derived radial velocities, we use a weighted average of the nine values to avoid any systematic offset that could be due to particular features in one of the templates. Hence, the Heliocentric radial velocity, v_r , of an observed star is given by

$$v_r = \left(\sum_{i=1}^{\text{nb temp}} \frac{1}{\sigma_i^2} \right)^{-1} \sum_{i=1}^{\text{nb temp}} \frac{v_{r,i}}{\sigma_i^2} \quad (1)$$

where $v_{r,i}$ is the radial velocity derived from the cross-correlation of the observed spectrum with the i th template and σ_i is the related uncertainty, given by the IRAF function FXCOR. To judge the homogeneity of the different $v_{r,i}$ around v_r , we also calculate the weighted dispersion, σ'_v , of the $v_{r,i}$ around v_r

$$\sigma_v'^2 = \left(\sum_{i=1}^{\text{nb temp}} \frac{1}{\sigma_i^2} \right)^{-1} \sum_{i=1}^{\text{nb temp}} \frac{(v_r - v_{r,i})^2}{\sigma_i^2}. \quad (2)$$

Stars with poorly determined radial velocities were eliminated by keeping only stars with $\sigma'_v < 5 \text{ km s}^{-1}$ which represent more than 90 per cent of our sample.

2.2 Reduction of second spectrograph spectra

Only RC stars were observed with the second spectrograph settings. It has been shown in Martin et al. (2005) that these settings produce no important deformation of the LSF and do not require the application of the reduction pipeline we used for spectrograph 1 data. For each star, we fit a Gaussian model for each of the three lines of the Ca II triplet and derive a velocity. We use the weighted average of these three velocity values as the radial velocity of the star and compute the weighted dispersion σ'_v . Stars with $\sigma'_v < 6.0 \text{ km s}^{-1}$ are kept as valid stars for the second spectrograph settings (once again this represents more than 90 per cent of the sample).

On both spectrographs, and to account for systematic offsets of no higher than $\sigma_{2dF} = 5 \text{ km s}^{-1}$ that may remain after applying our reduction pipeline, we increase the uncertainty σ'_v of each star to reach the total uncertainty σ_v on each radial velocities

$$\sigma_v = \sqrt{\sigma_v'^2 + \sigma_{2dF}^2}. \quad (3)$$

Finally, we note that the observed spectra are of sufficiently good quality to avoid significant variation of σ_v with the magnitude of the target stars (σ_v varies between 6 and 8 km s^{-1} over the $7 < K < 13$ range of our sample).

3 KINEMATIC RESULTS

3.1 Properties of the RGB sample at the centre of CMa

Our sample of RGB stars show no significant change with Galactic latitude hence, we merge the data of all the fields with $b < 0^\circ$. The distribution of radial velocities of the 228 RGB stars in these four CMa fields is shown on the top panel of Fig. 3 selected around the estimated distance to the structure ($5 \text{ kpc} < D_{\odot} < 11 \text{ kpc}$). The distribution is rather broad, but has a well-defined peak of stars at $\sim 115 \text{ km s}^{-1}$.

3.1.1 Comparison with the Martin et al. (2004b) results

In Paper III, we presented a similar analysis of the radial velocity of RGB stars near the centre of CMa based on only the two central fields of the present survey [$(l, b) = (240.0^\circ, -6.8^\circ)$ and $(l, b) =$

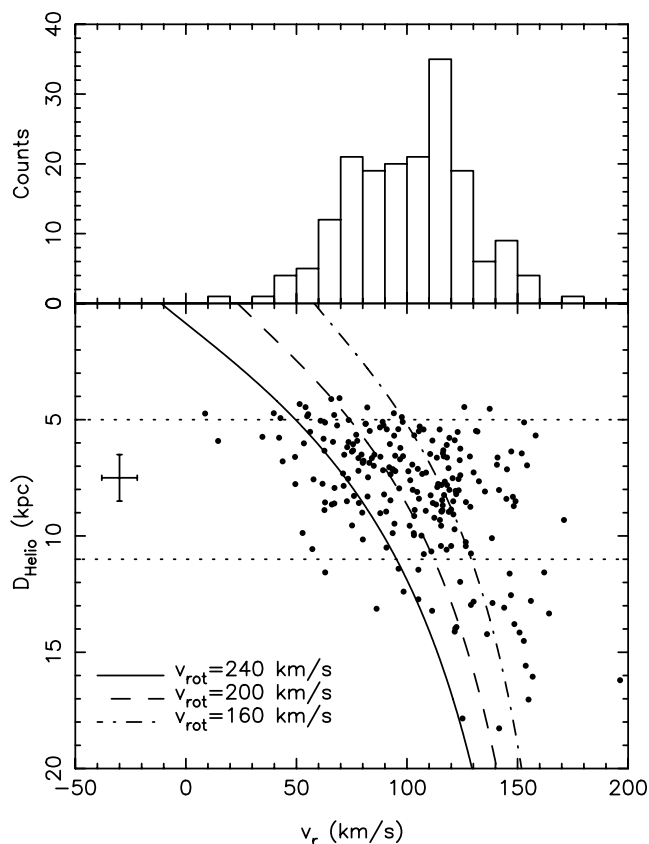


Figure 3. The top panel shows the radial velocity distribution of RGB stars near the centre of CMa (5 kpc < D_{\odot} < 11 kpc). A peak of stars is present at ~ 115 km s⁻¹. The lower panel shows the position of these RGB stars in phase space, with the typical error on both radial velocity and distance reported on the left. The peak is produced by a group of stars clustered between 7 kpc and 9 kpc. The expected position of a population orbiting the Milky Way in a circular orbit at $v_{\text{rot}} = 240$ km s⁻¹ (full line), $v_{\text{rot}} = 200$ km s⁻¹ (dashed line) and $v_{\text{rot}} = 160$ km s⁻¹ (dashed-dotted line) has been overplotted for comparison. The stars selected to produce the histogram of the upper panel are those between the two dotted line.

(240.0°, -8.8°)]. However, in that analysis the distribution of radial velocity showed two narrow peaks, centred on 60 and 110 km s⁻¹, that are not reproduced here. The second peak is visible on Fig. 3, but the first one has completely disappeared. This peak was in fact artificially produced by template issues resulting from a fluctuating LSF asymmetry during the different observation nights.

This is illustrated on Fig. 4 where, for one of the stars belonging to the first peak of Paper III, we present the radial velocities derived from the different observed templates (left panel) and those derived using the artificial templates to correct for the LSF asymmetry (right panel). Using our new reduction pipeline, most of the derived radial velocities are well clustered around v_r as defined in equation (1). Only two templates are over the 1σ limit but they have high radial velocity uncertainties and hence, are not significant in the determination of the combined v_r . On the other hand, the radial velocities derived for the different templates used in Paper III are widely scattered (over 35 km s⁻¹), and are not uniformly distributed. In particular, the two low uncertainty values are clustered around ~ 60 km s⁻¹ while all the other values are clustered not far from the new radial velocity derived by the pipeline. As in Paper III we only used the radial velocity that had the lowest uncertainty as the radial

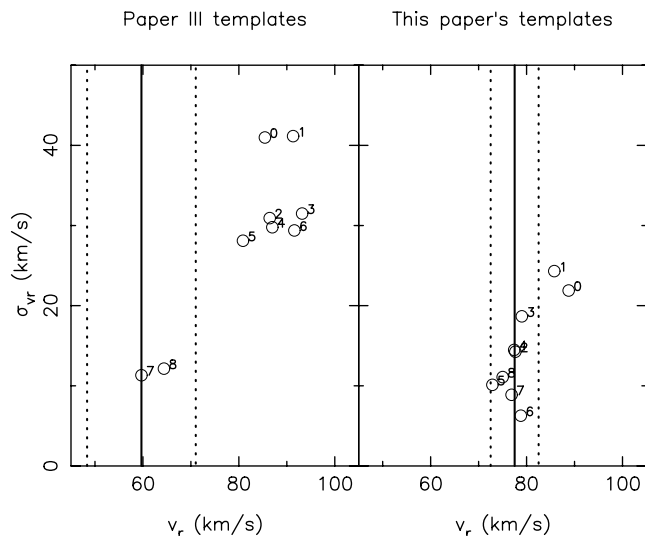


Figure 4. Distribution of the radial velocities produced by the different template of Paper III (left panel) and this paper (right panel) for the same RGB star. The thick lines represent the radial velocity used in the two papers and the dotted line represent the $\pm 1\sigma_v$ limit. The reduction pipeline used here yields much more clustered values than before. See the text for more details.

velocity of the studied star, this star (as well as multiple other ones) ended up artificially populating a peak of stars at ~ 60 km s⁻¹.

3.1.2 The CMa radial velocity signature

Looking at the position of the RGB stars in phase space (bottom panel of Fig. 3) reveals the peak in the distribution is produced by a clump of stars with $7.5 \text{ kpc} < D_{\odot} < 11.0 \text{ kpc}$. A more detailed analysis of this distance range (Fig. 5) reveals a population with a narrow dispersion. Comparing the data between 85 km s⁻¹ and 145 km s⁻¹ with a Gaussian model using a maximum likelihood technique reveals this population is centred on 114 ± 2 km s⁻¹ and has an intrinsic dispersion of 11^{+3}_{-1} km s⁻¹ when accounting for radial velocity uncertainties as in equation (3). As we explained previously in Paper III, the radial velocity of this population is not easily compatible with a disc-like population as it would be orbiting the Galaxy with a rotational velocity of only ~ 160 km s⁻¹. Given the distance and peculiar velocity of this population, we assume that it corresponds to the CMa dwarf. Changing the lower distance cut

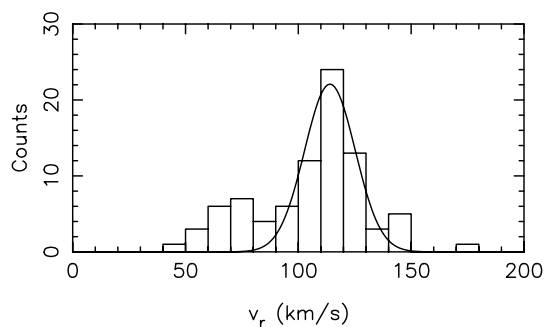


Figure 5. The radial velocity distribution of those stars within 7.5 and 11 kpc from the Sun in the four CMa fields. The peak in the distribution is well reproduced by a Gaussian model centred on 114 ± 2 km s⁻¹ and with an intrinsic dispersion of 11^{+3}_{-1} km s⁻¹.

in the range 7 kpc–8 kpc does not substantially modify these results (position and dispersion change by less than 2 km s^{-1}).

At closer distance, even though 2MASS starcounts of RGB stars betray the presence of the CMa dwarf (Paper III), most of the stars follow a more disc-like velocity. Yet, a group of these stars seems aligned in phase space, from $D_{\odot} \sim 6 \text{ kpc}$ and $v_r \sim 70 \text{ km s}^{-1}$ to the position of the clump of stars at higher distance. The low number of RGB stars in our sample prevents any firm conclusion on the reality of this feature, even though it seems to have a low dispersion. In the same distance range, a more diffuse group of stars also appears at higher radial velocity ($v_r > 140 \text{ km s}^{-1}$). Given the relatively sparse nature of these stars they could simply be the tail of the distribution of disc stars and/or could possibly represent a contamination from halo stars along these sight lines.

Another interesting feature of the phase space diagram is the group of stars at high distances (mainly $11 \text{ kpc} < D_{\odot} < 15 \text{ kpc}$ corresponding to $16.5 \text{ kpc} < D_{GC} < 20 \text{ kpc}$) that seems to be disconnected from the CMa population by a gap at $D_{\odot} \sim 11 \text{ kpc}$. The Galactic disc is known to possess a cut off at $D_{GC} \sim 15 \text{ kpc}$ (e.g. Ruphy et al. 1996) and hence, no disc stars are expected at the distance of this group. Moreover, given the high radial velocity of these stars, it seems unlikely that this group is composed of misidentified dwarfs. In fact, because these stars appear to be located between 16.5 and 20 kpc from the Galactic centre we believe we have uncovered part of the Monoceros Ring behind the CMa dwarf. The radial velocity signature of this population is compatible with previous work but we defer a more thorough analysis of the presence of the Monoceros Ring in all our low latitude fields to another contribution (Conn et al. 2005b).

3.2 The RC sample at the centre of CMa

Most of the RC stars were observed in the $(l, b) = (240.0^\circ, -8.8^\circ)$ field and should give a more precise view of the kinematics at the core of the CMa dwarf. While restricted to a shorter range in distance, the RC sample has the advantage of containing ~ 1350 stars at the distance of the group of RGB stars that seem to be aligned in phase space. The distribution of these RC stars in phase space (bottom panel of Fig. 6) presents a behaviour that is very similar to the RGB sample, with an overdensity of stars that follow a distance–radial velocity relation. The distributions of the radial velocity of these stars for 1 kpc bins are shown on the top panels of Fig. 6. We suspect two populations are present in each bin: contaminating stars that fall in our CMD selection box of RC stars and genuine CMa RC stars. To determine whether it is worth fitting a double Gaussian model to the distribution, we use the KMM test presented in Ashman, Bird & Zepf (1994). The probabilities P that the data are better represented by a single Gaussian instead of two are $P(5 < D_{\odot} < 6) = 1.0$, $P(6 < D_{\odot} < 7) = 6 \cdot 10^{-3}$ and $P(7 < D_{\odot} < 8) < 10^{-3}$ for the three distance bins. The last two bins are hence inconsistent with a single Gaussian model and only the closest one would be better characterized by a single Gaussian. However, because the distance–radial velocity relation still seems to be present in this bin, we believe that the two populations appear in this bin but that their mean velocity is located at around the same position. Hence, we proceed in fitting a double Gaussian model to the data in all bins, knowing that uncertainties on the derived values for the first bin will be large.

We use a maximum likelihood technique to fit the double Gaussian model. The uncertainties σ_v on each radial velocity were taken into account whereas no uncertainty was assumed for RC distance because the only important source of error comes from the absolute

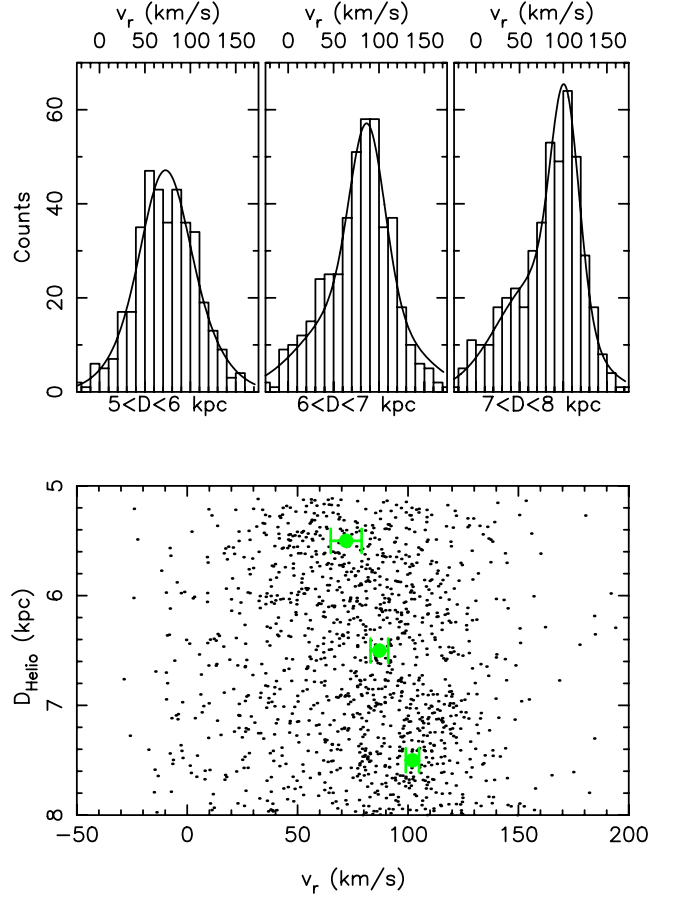


Figure 6. Phase space distribution of stars in the RC sample (bottom panel). A significant part of the stars follows a distance–radial velocity relation that is confirmed when analysing the radial velocity distribution of stars in 1 kpc bins (histograms of top panels, with the fits corresponding to the values of Table 2). The positions of this peculiar population have been overplotted as filled circles in the bottom panel, with error bars representing 1σ uncertainties on these values.

magnitude of the population and a change in this value would only shift the sample as a whole. As the two populations are most clearly separated in the $7 < D_{\odot} < 8 \text{ kpc}$, we use the stars in this bin to determine the proportion of RC stars that belong to the CMa population. The fit yields to a 40 per cent proportion of CMa stars, well within the 25–50 per cent determined by Bellazzini et al. (2004). As we expect this proportion to be roughly constant over our 3 kpc sample (see fig. 2 of Paper II), we also adopt this value for the two closest bins. The four parameters of the fits – mean velocity $\langle v_{r, \text{CMa}} \rangle$ and intrinsic dispersion σ_{CMa} of the CMa population and mean velocity $\langle v_{r, \text{cont}} \rangle$ and intrinsic dispersion σ_{cont} of the contaminating population – are presented in Table 2.

Table 2. Parameters of the RC radial velocity distribution fits. Columns 1 and 2 state, respectively, the mean velocity and the intrinsic dispersion of the CMa population. Columns 3 and 4 list the same parameters for the contaminating population.

Distance bin (kpc)	$\langle v_{r, \text{CMa}} \rangle$ (km s^{-1})	σ_{CMa} (km s^{-1})	$\langle v_{r, \text{cont}} \rangle$ (km s^{-1})	σ_{cont} (km s^{-1})
$5 < D_{\odot} < 6$	72 ± 7	24 ± 4	75 ± 6	42 ± 4
$6 < D_{\odot} < 7$	87 ± 4	20 ± 3	76 ± 5	54 ± 4
$7 < D_{\odot} < 8$	102 ± 3	16 ± 3	71 ± 5	46 ± 3

Each distance bin contains a low dispersion population with an increasing mean radial velocity and a broad population of constant mean velocity. This latter population shows a velocity dispersion σ_{cont} comparable to Solar neighbourhood velocity dispersions of the thick disc $(\sigma_U, \sigma_V, \sigma_W) = (63 \pm 6, 39 \pm 4, 39 \pm 4) \text{ km s}^{-1}$ (Soubiran, Bienaymé & Siebert 2003). We believe these stars are disc stars and dwarfs close to the Sun that fall in the RC region of the $(J - K, K)$ CMD and contaminate our sample. On the other hand, the other population that we believe to be composed of CMa stars is kinematically cold, with an intrinsic internal dispersion around $16 \pm 3 \text{ km s}^{-1}$. In the last bin, it is likely that the increase in σ_{CMa} in the other distance bins is only due to difficulties for the fit to disentangle the two populations. The other notable feature of these stars is their increasing radial velocity with distance, from $72 \pm 7 \text{ km s}^{-1}$ to $102 \pm 3 \text{ km s}^{-1}$ over only 3 kpc. Comparison with the group of RGB stars we identified as CMa stars at higher distance reveals striking similarities with both RC and RGB samples being kinematically cold and having compatible intrinsic dispersion. Moreover, the distance–radial velocity trend that appears in the RC sample is nicely prolonged to higher distances by the group of CMa RGB stars at $D_{\odot} \sim 8.5 \text{ kpc}$ and overlap with the group of RGB stars that seem to be align in phase space for the $D_{\odot} > 6 \text{ kpc}$ region. It is unlikely that a disc-like population could show characteristics that are similar to these stars given the high shift in radial velocity over only a few kiloparsecs. Indeed, if the considered population was rotating around the Milky Way on a circular orbit, it would have a rotational velocity as high as $v_{\text{rot}} \sim 220 \text{ km s}^{-1}$ at 5.5 kpc and as low as $v_{\text{rot}} \sim 160 \text{ km s}^{-1}$ at 8.5 kpc. On the other hand, correlation in phase space and low dispersion in radial velocity, two characteristics that the CMa population shows, are typical of an accretion process (see e.g. Ibata et al. 1997, for the Sgr dwarf).

To further test this conclusion, we compare the observations with the Besançon model (Robin et al. 2003). We simulate the J, H, K CMD of the region $239^\circ < l < 241^\circ$ and $-4^\circ < b < -12^\circ$, from which we extract RC stars with the same colour cuts as those we used to define our RC sample. We then calculate the distance to the stars in the model as we do for the observed stars, assuming an absolute magnitude of $M_K = -1.5$. Of course, because these stars do not belong to the CMa dwarf, their estimated distance is different from their distance provided by the model. From the ~ 150 stars in the model for the selected region, four fifths are in fact located at less than 1 kpc from the Sun. The distribution of these stars in phase space (Fig. 7) therefore represents that of the close disc stars that contaminate our sample of CMa RC stars. They do not follow the distance–radial velocity relation that we attributed to the CMa dwarf and are, on the contrary, located at a lower velocity. A similar behaviour is observed for RGB stars in the model.

3.3 The $(l, b) = (240.0^\circ, +8.8^\circ)$ field

Another check of the peculiar radial velocity of the stars in the CMa structure is given by the field that is symmetric to the CMa fields on the other side of the Galactic disc and that does not show the features that appear at the centre of the CMa dwarf (Fig. 8). The RGB sample for this field contains stars that are mostly located at $D_{\odot} < 6 \text{ kpc}$ with the expected radial velocity of a population orbiting the Milky Way at $v_{\text{rot}} \sim 200 \text{ km s}^{-1}$. Only 11 stars fall within the distance cut that was used to produce Fig. 5 near the centre of CMa. Moreover, the remaining stars at higher distances show no sign of clustering. The RC stars in this field follow a broad distribution with a dispersion of $\sim 50 \text{ km s}^{-1}$, centred around $\sim 60 \text{ km s}^{-1}$ over the 3 kpc sample,

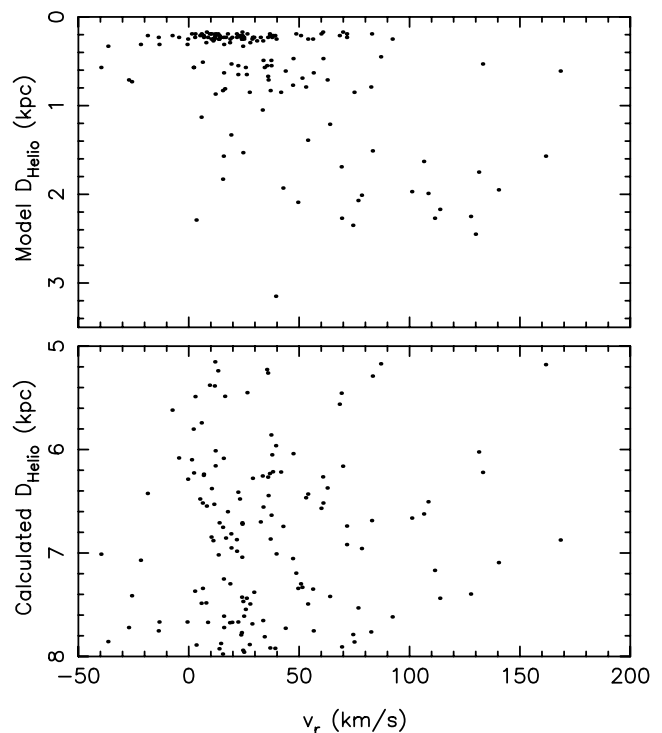


Figure 7. Phase space distribution of stars in the Besançon model that fall in our selection box for RC stars in the region of the observed 2dF fields. For the top panel, the distance of the stars in the model was used and shows that most of the contamination in the observed sample is due to stars close to the Sun. For the bottom panel, we calculate the distance as we do for the observed sample of RC stars. A direct comparison of this panel with Fig. 6 shows that the distance–radial velocity relation in our sample is not predicted by the model.

similar to what we identify as the contaminating population in the CMa field, and also similar to what would be expected from close stars artificially spread over the 3 kpc distance range. Therefore, the peculiar features that appear at the centre of CMa have to be due to the CMa population.

4 UCAC2.0 PROPER MOTIONS OF THE CANIS MAJOR DWARF

Momany et al. (2004) used the UCAC2.0 catalogue (Zacharias et al. 2004) to show that the CMa overdensity of RGB stars rotates around the Galaxy in a prograde motion. However, given the sizable uncertainties on the proper motion values of individual stars and the contamination of disc stars in the sample, they were only able to give a rough estimate of the proper motions that convert in Galactic coordinates as: $\mu_l = -3.5 \text{ mas yr}^{-1}$ and $\mu_b = -0.1 \text{ mas yr}^{-1}$ with uncertainties of $\sim 2.0 \text{ mas yr}^{-1}$.

With the addition of radial velocities of stars in the direction of CMa, we are now in a position to define a less contaminated sample of stars that belong to the dwarf. We first determine the best linear fit to the distance–radial velocity relation of the RC sample by using the three radial velocity measurements for the three distance bins. We then extract from UCAC2.0 the proper motions of the RC stars that are located within $\pm 10 \text{ km s}^{-1}$ of this linear fit. This selection should ensure that a sizable proportion of our objects indeed belong to the CMa dwarf. To account for the distance D_{\odot} of the different stars, we normalize each proper motion μ_{UCAC} as if the star was

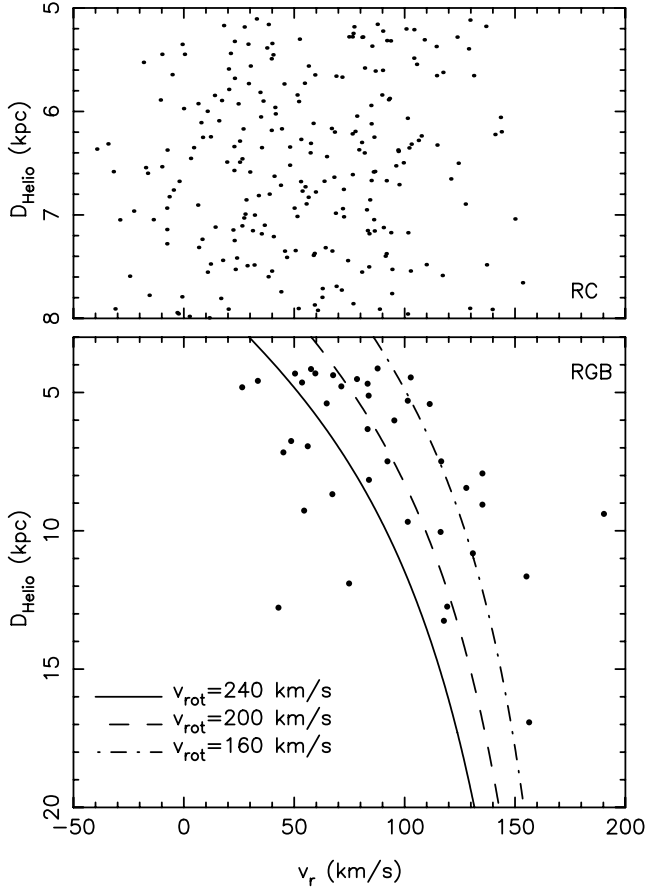


Figure 8. Phase space distribution of RC (top panel) and RGB stars (bottom panel) in the $(l, b) = (240.0^\circ, +8.8^\circ)$ field. Neither of the two shows the features that are present in fields centred on the CMa dwarf galaxy.

located at the Heliocentric distance of the CMa dwarf ($D_{\odot, \text{CMa}} = 7.2 \text{ kpc}$)

$$\mu = \mu_{\text{UAC}} \cdot \frac{D_{\odot}}{D_{\odot, \text{CMa}}}. \quad (4)$$

The distribution of these μ proper motions is shown on the bottom left panel of Fig. 9 and is consistent with the Momany et al. (2004) measurements.

We use a maximum likelihood technique to determine the best fit of this distribution by a two-dimensional Gaussian function. The best mean values are $(\bar{\mu}_l, \bar{\mu}_b) = (-2.5 \text{ mas yr}^{-1}, 1.5 \text{ mas yr}^{-1})$ with internal dispersions of $(\sigma_{\mu_l}, \sigma_{\mu_b}) = (4.8 \text{ mas yr}^{-1}, 3.7 \text{ mas yr}^{-1})$. To analyse in more depth the proper motions of the CMa population, we use these values to eliminate outliers and study the μ_l distribution of stars within σ_{μ_b} of $\bar{\mu}_b$ (top panel of Fig. 9) and the μ_b distribution of stars within σ_{μ_l} of $\bar{\mu}_l$ (right panel of Fig. 9). This latter distribution is well centred around $\bar{\mu}_b$ (the arrow) and the value $1.5 \pm 0.5 \text{ mas yr}^{-1}$ can be taken as the proper motion of the CMa dwarf in Galactic latitude. On the other hand, the distribution of proper motions in Galactic longitude is not centred around $\bar{\mu}_l$. A peak appears at lower proper motion, with a wing that extends to positive values. Considering that, even with our cut in radial velocity, contaminating stars from the disc should still be in our sample of stars, we use a maximum likelihood technique to fit a double Gaussian model to the distribution (the KMM test yields a low probability of 10^{-2} that the population is better represented by a single Gaussian). This reveals two distinct populations are present: similar

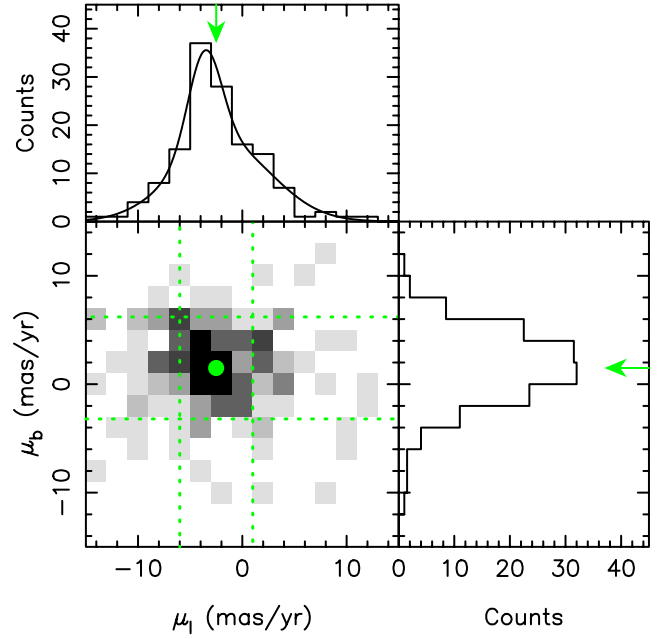


Figure 9. The bottom left panel shows the distribution in proper motion space of CMa RC stars selected along the distance–radial velocity feature of Fig. 6. A black pixel corresponds to eight stars. The centre of the distribution (assuming Gaussian distributions) is overplotted as a dot. The distribution of those stars within 1σ of this point in the μ_b (respectively μ_l) direction was used to produce the distribution of CMa stars in μ_l (respectively μ_b) on the top (respectively right) panel. The mean positions derived from the Gaussian fits of the whole distribution are shown as arrows. A wing in the distribution in μ_l betrays the presence of two populations that we fit by a double Gaussian model.

to what was observed in radial velocity, one has a large dispersion (4.7 mas yr^{-1}), is centred on $\mu_l = -1.9 \text{ mas yr}^{-1}$ and accounts for one fourth of the total number of stars while the other has a much narrower dispersion ($1.5 \pm 0.4 \text{ mas yr}^{-1}$) and is centred on $\mu_l = -3.6 \pm 0.8 \text{ mas yr}^{-1}$. As one expects the contaminating stars in the sample to be at different distances and hence have different proper motions, we believe the broad population corresponds to these stars; so the narrow population has to be due to the CMa dwarf.

For comparison, we show on Fig. 10 the distribution of RC stars in our sample that are more than $\pm 20 \text{ km s}^{-1}$ away from the linear fit of the CMa radial velocity and that should correspond to the contaminating population in the sample. This population has a proper motion of $(\mu_{l, \text{cont}}, \mu_{b, \text{cont}}) \sim (-2.0 \text{ mas yr}^{-1}, 2.0 \text{ mas yr}^{-1})$ offset from the CMa proper motion, especially for the proper motion in Galactic longitude.

The derived proper motion values for the CMa dwarf $(\mu_l, \mu_b) = (-3.6 \pm 0.8 \text{ mas yr}^{-1}, 1.5 \pm 0.4 \text{ mas yr}^{-1})$ are compatible with the Momany et al. (2004) values but with much lower uncertainties. Correcting from the reflex solar motion along the line of sight yields $(\mu'_l, \mu'_b) = (-6.8 \pm 0.8 \text{ mas yr}^{-1}, 0.8 \pm 0.4 \text{ mas yr}^{-1})$, corresponding to a tangential velocity of 234 km s^{-1} at the mean distance of 7.2 kpc .

5 SIMULATIONS

The kinematic information on the CMa dwarf provides interesting constraints on the accretion process that the dwarf is undergoing. In this section, we revisit the simulations of Paper I, this time using only constraints that can be directly linked to CMa. Indeed, because there is no definite proof of a link between CMa and the Mon Ring,

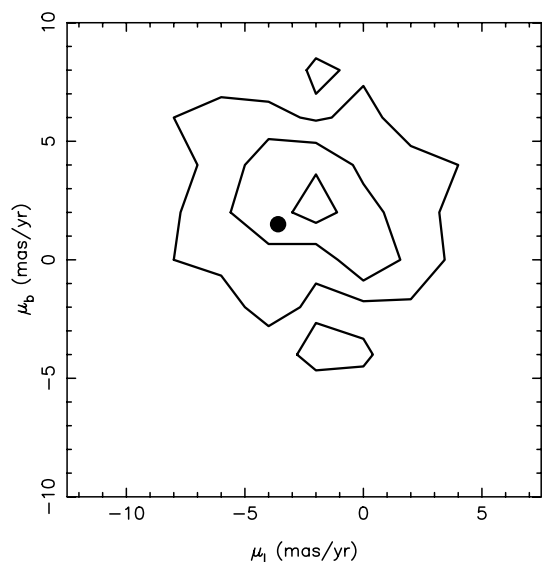


Figure 10. The contours show the distribution of RC stars in our sample that are more the 20 km s^{-1} away from the distance–radial velocity relation followed by CMa stars. This population is centred around $(\mu_{l,\text{cont}}, \mu_{b,\text{cont}}) \sim (-2.0 \text{ mas yr}^{-1}, 2.0 \text{ mas yr}^{-1})$ and offset from the CMa population whose mean proper motion is represented by the black dot.

we choose not to use the numerous kinematic and/or positional data on the Mon Ring for our simulations.²

The simulations are performed in the same way as in Martin et al. (2004a), using the fast and momentum-conserving tree code integrator FALCON (Dehnen 2000, 2002). The simulation that best fits the kinematic data at the centre of CMa is shown from the North Galactic Pole on Fig. 11. It is produced by a dwarf galaxy modelled by a King model of $5 \times 10^8 M_{\odot}$ with a tidal radius of 2.7 kpc and $W_0 = 3.25$ and that is accreted on to the Milky Way during ~ 3 Gyr. The simulation reproduces at the same time the overdensity of stars that revealed the dwarf in 2MASS, the proper motions we measured in this paper (with values of $\mu_l \sim -4 \text{ mas yr}^{-1}$ and $\mu_b \sim 2 \text{ mas yr}^{-1}$) and, above all, the distance–radial velocity gradient that appears in RC (and possibly RGB) stars. This is shown on Fig. 12, with the values measured in this paper plotted as squares and triangle on top of the particles of the simulation in the region of our 2dF fields. Moreover, the velocity dispersion of the particles reproduces that measured for the RGB sample (11 km s^{-1}). Of course, the parameters of the initial dwarf are certainly not the only ones that can reproduce the radial velocities at the centre of the dwarf but it should be noticed that the simulated position and velocities are very near what is observed.

The group of particles that is visible at higher distance ($9 \text{ kpc} < D < 12 \text{ kpc}$) is produced by one of the tidal arms of the dwarf that is wrapped a few times around the Milky Way. Even if the group is not exactly at the same distance as what we identify as the Mon Ring behind the CMa dwarf, it is tempting to explain the two observations by the same accretion process. It is also interesting

² Moreover, the existence of the Mon Ring behind CMa seems to hint against a direct link between the two structures and it would be the tidal arms of the dwarf, wrapped a few times around the Galaxy, that would produce the ring-like structure. If such a scenario is plausible (see e.g. Peñarrubia et al. 2005), the constraints provided by the Ring data on the accretion parameters of the dwarf are weak.

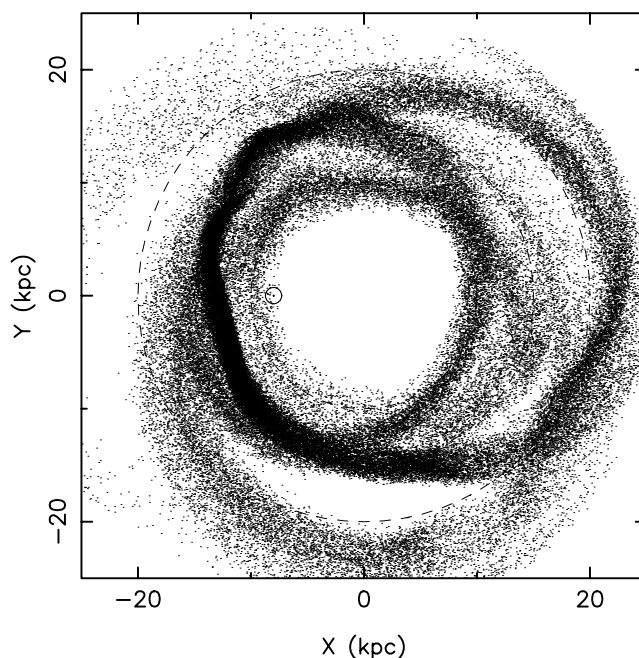


Figure 11. Our best simulation of the accretion of the CMa dwarf viewed from the North Galactic Pole. The Sun is represented by a dotted circle and the three dashed circles represent distances of 10, 15 and 20 kpc from the Galactic centre. The main body of the CMa dwarf is visible at $(X, Y) \sim (-12 \text{ kpc}, -6 \text{ kpc})$ and the tidal arms produced by the accretion are wrapped multiple times around the Milky Way.

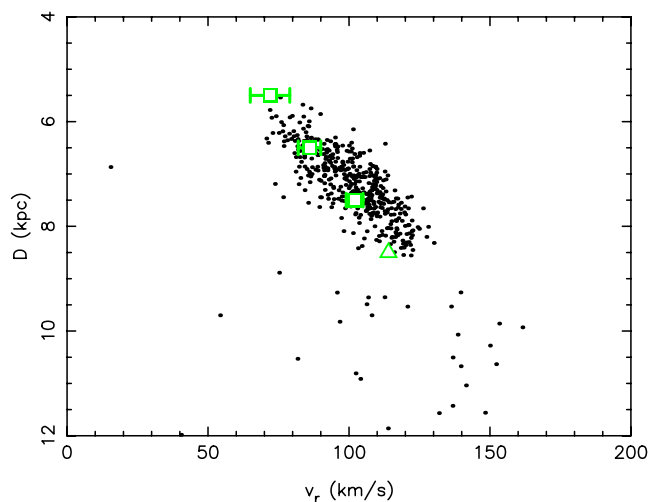


Figure 12. Distribution in space phase of the particles (dots) of our best simulation at the location of the 2dF fields we present in this work ($239^\circ < l < 241^\circ$ and $-12^\circ < b < -4^\circ$). The observed values of radial velocity are shown as squares for values derived from the RC sample and a triangle for the one derived from the RGB sample. They are well matched by the particles. The group of star at higher distances is produced by the multiple wraps of the tidal arms of the dwarf around the Milky Way.

to notice that the average location of these tidal arms in Fig. 11 are close to the distance range of the Mon Ring ($10 \text{ kpc} < D_{\text{GC}} < 18 \text{ kpc}$ in the anticentre direction) while the radial velocity of the arm reveals it is only shifted by $\sim 30 \text{ km s}^{-1}$ compared to the SDSS radial velocities of Yanny et al. (2003). The more distant portions of the arms that extend at 20–30 kpc from the Galactic centre could also

explain the Triangulum–Andromeda structure presented in Rocha-Pinto et al. (2004). Yet, given the lack of definitive proof of a link between the two structures, we chose not to try to fit the radial velocity of the group of Mon Ring stars behind CMa. Indeed, a small shift of $\sim 10 \text{ km s}^{-1}$ in the tangential velocities of our simulation substantially changes the position and kinematics of the tidal arms. Only with a determination of the radial velocity of the arms away from the main body of the dwarf could such a constraint be useful.

6 CONCLUSION

We have shown that the RGB and RC stars at the centre of the CMa dwarf have peculiar kinematics that are incompatible with a disc-like population.

(i) The phase space distribution of stars (whether RGB or RC) in the CMa fields under the Galactic disc (Figs 3 and 6) is very different from that of the symmetric region on the other side of the disc (Fig. 8).

(ii) More than one third of the stars in the RC sample follow a distance–radial velocity relation over all the sample ($5 \text{ kpc} < D_{\odot} < 8 \text{ kpc}$). This relation seems also to be present in the RGB sample and prolonged to higher distances by a group of RGB stars. The important radial velocity shift over only a few kiloparsecs for these stars (which is not reproduced by the Besançon Galactic model) cannot be explained by a group of stars rotating around the Milky Way on a circular orbit.

(iii) The proper motions of the dwarf that we derived from the UCAC2.0 catalogue (μ_l, μ_b) = $(-3.6 \pm 0.8 \text{ mas yr}^{-1}, 1.5 \pm 0.4 \text{ mas yr}^{-1})$ yields at tangential velocities when corrected from the Solar motion of $(v_l, v_b) = (-235 \pm 35 \text{ km s}^{-1}, +15 \pm 25 \text{ km s}^{-1})$. Combined with a mean radial velocity of $v_r \sim -105 \text{ km s}^{-1}$ (also corrected from the Solar motion), the total velocity of the CMa population is $v_{\text{tot}} \sim 260 \text{ km s}^{-1}$ which is high compared to expectations for disc stars (e.g. Soubiran et al. 2003).

(iv) Both the RGB and the RC samples show the CMa population is kinematically cold, with intrinsic dispersions of 11 and 16 km s^{-1} respectively but this latter value may be overestimated due to the difficulty of separating CMa stars from contaminating stars in the RC sample. Such low dispersions are typical of recent accretion process and can be observed, for instance, in the Sagittarius dwarf galaxy (Ibata et al. 1997).

(v) Following the discovery of a distance spiral arm at the edge of the Galactic disc by McClure-Griffiths et al. (2004), we mentioned in Paper III, that the radial velocity of the CMa RGB population could be compatible with this spiral arm. However, the distance–radial velocity of RC CMa stars reach a much lower value of 72 km s^{-1} hardly compatible with the McClure-Griffiths et al. (2004) values. Moreover, H I maps do not show any hint of a spiral arm at the distance of the CMa object (see e.g. Nakanishi & Sofue 2003).

All these observations point at the accretion scenario for the CMa population, with a dwarf galaxy that is currently being absorbed by the Milky Way. The low-velocity dispersion suggests that, even though it is undergoing dramatic tidal stripping by our Galaxy, the dwarf is still bound. But can the CMa dwarf be also responsible for the Monoceros Ring and the Triangulum–Andromeda structure? If simulations can reproduce the observed kinematic signature of CMa, constraints on the tidal arms of the dwarf are at the moment not strong enough to definitely conclude on the CMa dwarf being the progenitor of the Mon Ring.

A definite conclusion may only come with future observations which should concentrate on mapping the regions around the centre

of dwarf ($220^\circ \lesssim l \lesssim 260^\circ$ and $-20^\circ < b < 0^\circ$). Moreover, in addition to constraining the orbit of the accretion, determining the intrinsic dispersion of the CMa population and the evolution of this dispersion around its core should allow a much more precise estimate of the parameters of the initial dwarf, as well as an estimate of its mass-loss rate (Johnston, Sigurdsson & Hernquist 1999).

ACKNOWLEDGMENTS

The referee is thanked for many useful comments that helped improve the overall quality of the paper.

REFERENCES

- Ashman K. M., Bird C. M., Zepf S. E., 1994, *AJ*, 108, 2348
 Bagnulo S., Jehin E., Ledoux C., Cabanac R., Melo C., Gilmozzi R., The ESO Paranal Science Operations Team, 2003, *The Messenger*, 114, 10
 Bellazzini M., Ibata R. A., Monaco L., Martin N. F., Irwin M. J., Lewis G. F., 2004, *MNRAS*, 354, 1263 (Paper II)
 Bonifacio P., Monai S., Beers T., 2000, *AJ*, 120, 2065
 Conn B. C., Lewis G. F., Irwin M. J., Ibata R. A., Irwin M. J., Ferguson A., Tanvir N., 2005a, *MNRAS*, in press (astro-ph/0506522)
 Conn B. C., Martin N. F., Lewis G. F., Ibata R. A., Bellazzini M., Irwin M. J., 2005b, submitted
 Crane J., Majewski S., Rocha-Pinto H., Frinchaboy P., Skrutskie M., Law D., 2003, *ApJ*, 594, L119
 Dehnen W., 2000, *ApJ*, 536, L39
 Dehnen W., 2002, *J. Comput. Phys.*, 179, 27
 Dehnen W., Binney J., 1998, *MNRAS*, 298, 387
 Ibata R., Wyse R., Gilmore G., Irwin M., Suntzeff N., 1997, *AJ*, 113, 634
 Ibata R., Irwin M., Lewis G., Ferguson A., Tanvir N., 2003, *MNRAS*, 340, 21
 Johnston K. V., Sigurdsson S., Hernquist L., 1999, *MNRAS*, 302, 771
 McClure-Griffiths N., Dickey J., Gaensler B., Green A., 2004, *ApJ*, 607, L127
 Majewski S., Skrutskie M., Weinberg M., Ostheimer J., 2003, *ApJ*, 599, 1082
 Martin N. F., Ibata R. A., Bellazzini M., Irwin M. J., Lewis G. F., Dehnen W., 2004a, *MNRAS*, 348, 12 (Paper I)
 Martin N. F., Ibata R. A., Conn B. C., Lewis G. F., Bellazzini M., Irwin M. J., McConnachie A. W., 2004b, *MNRAS*, 355, L33 (Paper III)
 Martin N. F., Ibata R. A., Conn B. C., Irwin M. J., Lewis G. F. 2005, *Publ. Astron. Soc. Aust.*, in press (astro-ph/0503703)
 Martínez-Delgado D., Butler D. J., Rix H.-W., Franco Y. I., Peñarrubia J., 2005, *ApJ*, in press (astro-ph/0410611)
 Momany Y., Zaggia S., Bonifacio P., Piotto G., De Angeli F., Bedin L., Carraro G., 2004, *A&A*, 421, L29
 Nakanishi H., Sofue Y., 2003, *PASJ*, 55, 191
 Newberg H. et al., 2002, *ApJ*, 569, 245
 Peñarrubia J. et al. 2005, *ApJ*, 626, 128
 Robin A., Reylé C., Derrière S., Picaud S., 2003, *A&A*, 409, 523
 Rocha-Pinto H., Majewski S., Skrutskie M., Crane J., Patterson R., 2004, *ApJ*, 615, 732
 Ruphy S., Robin A., Epchtein N., Copet E., Bertin E., Fouque P., Guglielmo F., 1996, *A&A*, 313, L21
 Schlegel D., Finkbeiner D., Davis M., 1998, *ApJ*, 500, 525
 Soubiran C., Bienaymé O., Siebert A., 2003, *A&A*, 398, 141
 Taylor K., Bailey J., Wilkins T., Shortridge K., Glazebrook K., 1996, in Jacoby G. H., Barnes J., eds, *ASP Conf. Ser. Vol. 101, Astronomical Data Analysis Software and Systems V*, p. 195
 Yanny B., Newberg H. et al., 2003, *ApJ*, 588, 824
 Zacharias N., Urban S. E., Zacharias M. I., Wycoff G. L., Hall D. M., Monet D. G., Rafferty T. J., 2004, *AJ*, 127, 3043

This paper has been typeset from a \LaTeX file prepared by the author.